Journal of Advanced Ceramics
先进陶瓷
ISSN 2226-4108
CN 10-1154/TQ
清华大学出版社 Tsinghua University Press
SciOpen

*J Adv Ceram* 2026, **15**: 9221410

https://doi.org/10.26599/JAC.2026.9221410

Research Article

# Beyond thermodynamic stability: oxygen penetration kinetics and oxide-scale integrity jointly govern the oxidation resistance of medium-entropy carbides

Chenyi Xie, Huaming Miao, Weiran Zhang, Yanfei Wang*, Duan Li, Rongjun Liu*

*Science and Technology on Advanced Ceramic Fibers and Composites Laboratory, College of Aerospace Science and Engineering, National University of Defense Technology, Changsha 410073, China*

*Corresponding author.

E-mail: Y. Wang, wangyanfei@nudt.edu.cn;

R. Liu, rongjunliu@163.com

Received: September 17, 2026; Revised: November 2, 2026; Accepted: November 18, 2026

©The Author(s) 2026

Just Accepted

清华大学出版社 Tsinghua University Press | SciOpen

**Abstract:** Selection of medium-entropy carbide ceramics has long relied on empirical trial and error and on thermodynamic criteria, yet whether such criteria can predict the oxidation resistance of a

material has rarely been examined. Here, ten Ti/Zr/Hf/Nb/Ta-based ternary carbide systems were screened by thermodynamic calculation, and three candidates were selected and oxidized. (TiZrHf)C, although the least stable of the three in thermodynamic terms, shows the best oxidation resistance, owing to its large surface-to-interstitial energy difference (5.927 eV) and to the dense oxide scale it develops. (TiHfTa)C has the most negative formation energy, but its multiphase scale accumulates pores and cracks at high temperature, which disrupt the continuity and density of the scale, may ease oxygen transport into the substrate, and eventually causes pronounced structural degradation. (ZrHfTa)C fails catastrophically through short-circuit diffusion along through-thickness cracks that form early in oxidation. Oxidation resistance is therefore not determined by thermodynamic stability alone, but by the interplay between oxygen penetration kinetics and the microstructure of the oxide scale. These results expose the limits of a single thermodynamic screening criterion and offer a combined framework for designing oxidation-resistant medium-entropy carbide ceramics.

**Keywords:** medium-entropy carbide, first-principles calculation, oxidation behavior, spark plasma sintering, phase stability.

Just Accepted

## 1 Introduction

Advances in aerospace technology and high-speed flight place increasingly demanding requirements on high-temperature thermal protection materials [1–3]. In environments that combine ultra-high temperature, strongly oxidizing atmospheres and high-velocity gas flow, a material must offer thermal stability, oxidation resistance and adequate load-bearing capacity at the same time [4–7]. Ultra-high-temperature ceramics (UHTCs), with their exceptionally high melting points and hardness, are among the most promising candidates for thermal protection [8–10], and appreciable progress has been made in their processing and properties [11–14]. High-entropy ceramics have attracted attention through their high-entropy and lattice-distortion effects, which give them advantages over

conventional single-component ceramics in thermal stability, oxidation resistance and mechanical performance. Their wider use, however, is constrained by the large number of constituent elements, by processing complexity and by the difficulty of controlling compositional homogeneity [15–20].

Against this background, medium-entropy ceramics have emerged as an important derivative of high-entropy ceramics. Typically built from three or four principal metal elements, medium-entropy ceramics retain the property advantages of multi-principal systems while easing processing and compositional control, and have become an active topic in the UHTC field [21]. Medium-entropy carbides (MECs) in particular combine high melting points with good thermal stability and oxidation resistance, owing to the strong metal–carbon bonding, and are therefore attractive for thermal protection. Reported compositions fall into seven ternary systems — (TiZrHf)C [22–39], (TiZrTa)C [40–43], (HfNbTa)C [44–46], (TiZrNb)C [47,48], (ZrNbTa)C [49,50], (ZrHfTa)C [46,51] and (TiHfTa)C [46,52] — yet most work is concentrated on (TiZrHf)C, while the properties of (TiTaNb)C, (TiHfNb)C and (ZrHfNb)C remain unexplored. Selecting oxidation-resistant compositions from this large space is still a central problem in the design of MECs.

Thermodynamic parameters such as the formation energy, the mixing enthalpy and the Gibbs free energy of the oxidation reaction are widely used to assess the phase stability and oxidation tendency of multi-component carbides. The reasoning is straightforward: the more negative the formation energy, the higher the thermodynamic stability; the weaker the driving force for oxidation, the less readily the material oxidises [52–54]. Thermodynamic calculation can therefore narrow the range of candidate compositions at an early stage, which is a clear advantage over empirical trial and error. The actual oxidation of a carbide, however, involves oxygen adsorption, oxide formation and phase change, inward oxygen transport, and the nucleation of pores and cracks. Treating thermodynamic stability as a proxy for oxidation resistance may therefore misrepresent the differences between MECs that behave very differently in practice.

Just Accepted

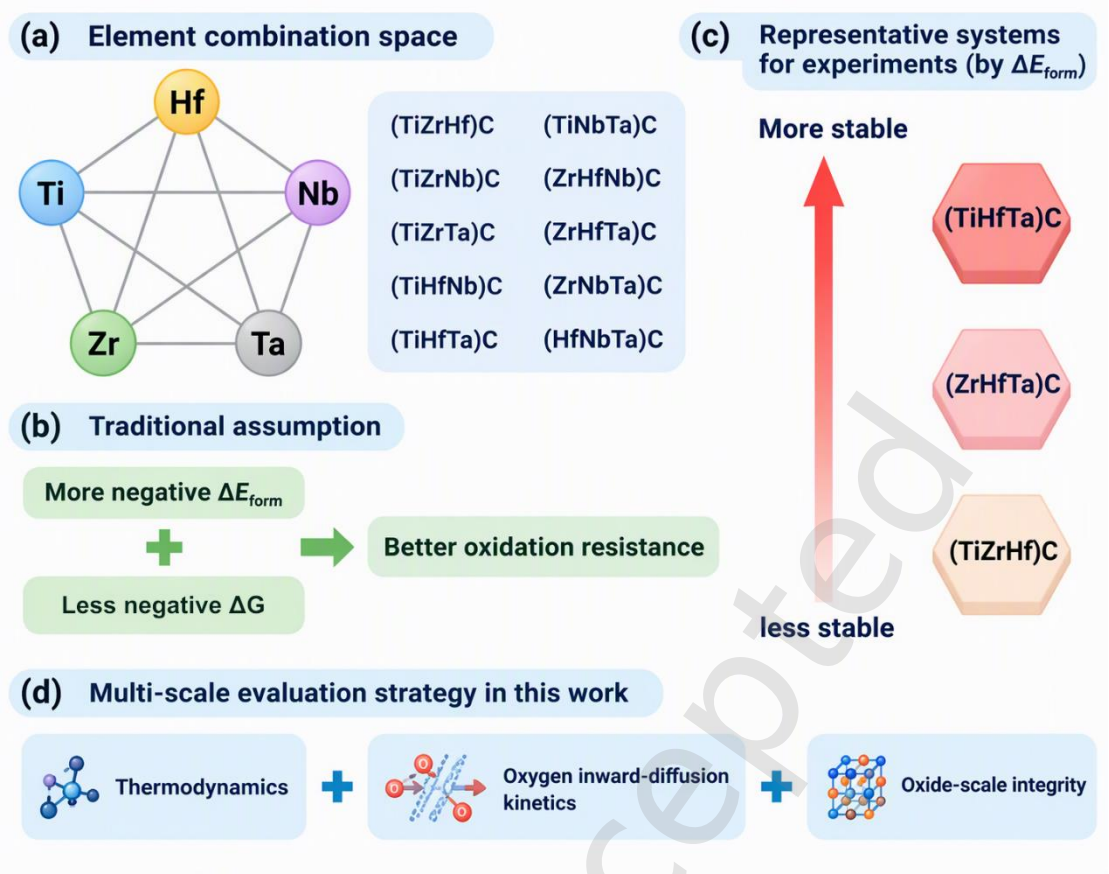



**Fig. 1** Framework of the present work: (a) the ten ternary MECs formed by Ti, Zr, Hf, Nb and Ta; (b) conventional thermodynamic screening logic; (c) the representative systems selected for experimental validation; (d) the assessment criteria adopted in this study.

To address these issues, we take the ten ternary MECs formed by Ti, Zr, Hf, Nb and Ta as the candidate space (Fig. 1(a)), select three representative systems on the basis of thermodynamic calculation (Fig. 1(c)) and examine them experimentally. Oxidation kinetics, the phase composition of the oxide scale and its microstructure are combined to compare the oxidation behavior and failure modes of the three materials, while first-principles calculations provide the surface adsorption energy of oxygen and the barrier for its penetration from the surface to the subsurface, so as to rationalize the differences between them. Three questions are addressed: whether conventional thermodynamic criteria predict the oxidation resistance of MECs (Fig. 1(b)); how inward oxygen transport and scale defects produce the deviation between prediction and experiment; and whether a combined screening criterion can be established for composition design (Fig. 1(d)).

Just Accepted

# 2 Experimental procedures

## 2.1 Theoretical calculation methods and processes

The first-principles calculations in this work were performed within the framework of density functional theory (DFT) using the Vienna Ab initio Simulation Package (VASP). Chemical disorder on the metal sublattice was modelled with the special quasirandom structure (SQS) method. The rock-salt structure of TiC was taken as the reference configuration, on the basis of which a $2 \times 2 \times 3$ supercell was constructed and the metal sites were occupied by the SQS approach, so that the statistical distribution of a real random alloy is reproduced as closely as possible within the finite supercell. The migration of an oxygen atom from a surface adsorption site to a subsurface interstitial site was examined with the climbing-image nudged elastic band (CI-NEB) method implemented in VASP. The calculation parameters and details are given in the Supplementary Information and in Fig. S1-2.

## 2.2 Preparation of MECs

Commercially available TiC, HfC, TaC and ZrC powders (500 nm; Hebei Canen Research New Materials Co., Ltd., China) were mixed in the required proportions and mechanically milled. The mixture was pre-treated at 1600 ℃ under vacuum and then consolidated by spark plasma sintering, with heating at 100 ℃/min to 1400 ℃, followed by 50 ℃/min to 2000 ℃, a holding time of 10 min and an applied pressure of 50 MPa, which yielded discs 30 mm in diameter. The discs were ground on abrasive paper to remove the carbon layer left on the surface and cut into 3×3×5 mm bars for the isothermal oxidation tests. For brevity, the (TiZrHf)C, (TiHfTa)C and (ZrHfTa)C are denoted TZH, THT and ZHT, respectively.

## 2.3 Characterization

Density and open porosity were measured by the Archimedes water-displacement method. Phase analysis of the bulk ceramics and of the oxide scales was carried out by X-ray diffraction (XRD; D8 Advance, Bruker AXS, Germany) with Cu Kα radiation at 40 kV and 200 mA, over a 2θ range of 10–90° and at a scan rate of 10°/min. The microstructure of the ceramics and of their oxidation products

Just Accepted

was examined by scanning electron microscopy (SEM; MIRA3, TESCAN Brno, s.r.o.) and energy-dispersive X-ray spectroscopy (EDS; Oxford Instruments).

Isothermal oxidation was performed in a thermal-shock furnace at 1000, 1200, 1300 and 1400 ℃. The furnace was heated to the target temperature at 15 ℃/min, and the specimens were then held in it for 20 min; one specimen was withdrawn every 20 min, the last one after a cumulative exposure of 120 min. Each specimen was weighed on an analytical balance before and after oxidation.

Pores and cracks in the SEM images of the oxide scales were analyzed with ImageJ; the calculation procedure is described in the Supplementary Information, together with the methods used to derive the thermal stress, the PBR and the density.

## 3 Results and discussion

### 3.1 Discrepancy between thermodynamic prediction and oxidation experiments

To assess the effectiveness of conventional thermodynamic indicators in screeningMECs, the average atomic formation energy $\Delta E_{\mathrm{form}}$ and the Gibbs free energy $\Delta G(T)$ of the oxidation reaction were first calculated for the ten systems (Fig. S3). TZH, THT and ZHT ceramics were then prepared and oxidized (characterization of the ceramic samples is given in Figs. S4 and S5). As shown in Fig. 2, the comparison between calculation and experiment indicates that, although thermodynamic calculation distinguishes the systems in terms of thermodynamic stability and driving force for oxidation, its predictions do not translate directly into oxidation resistance.

Just Accepted

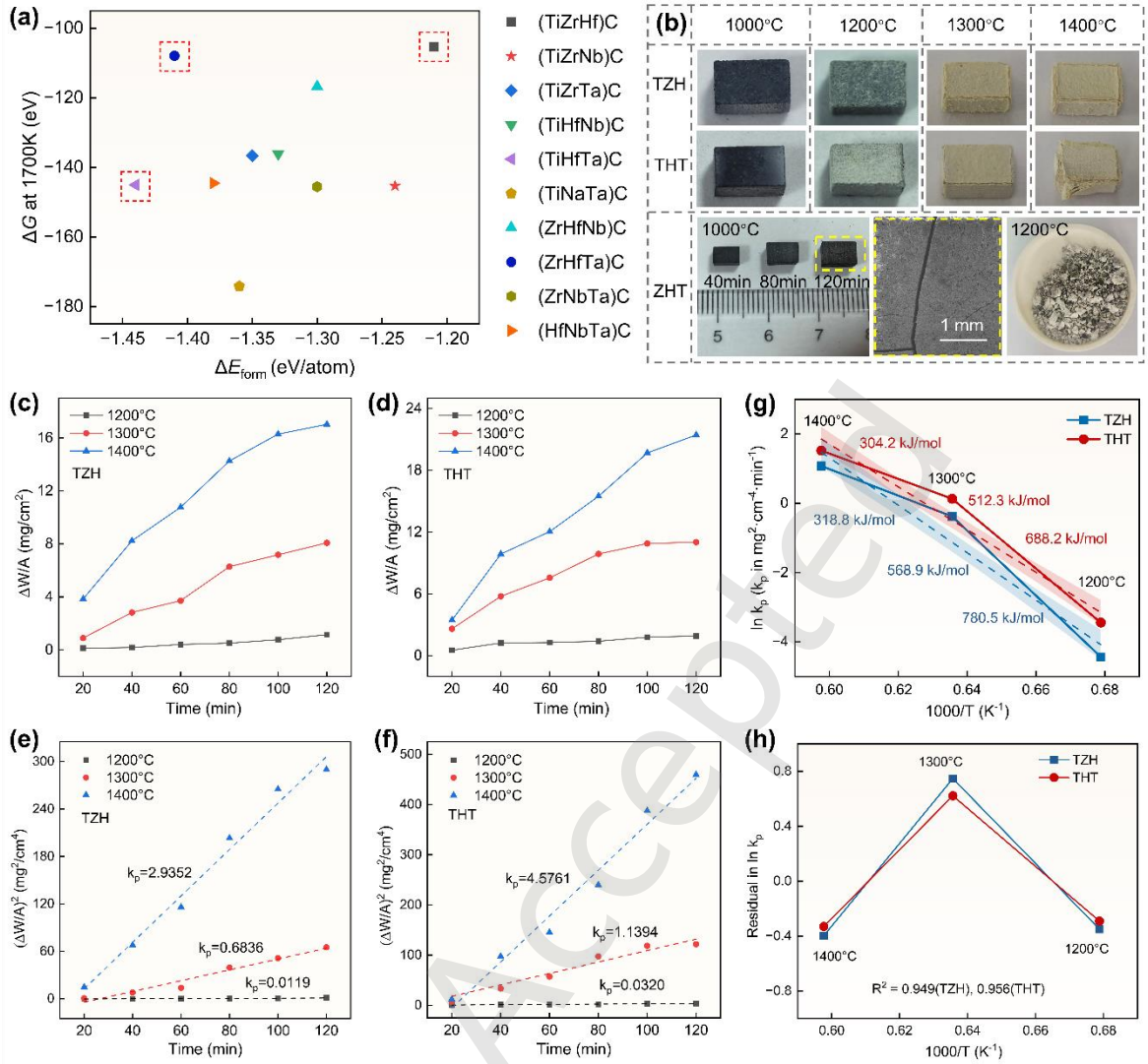



**Fig. 2** Thermodynamic calculations and oxidation experiments: (a) $\Delta E_{\mathrm{form}}$ versus $\Delta G(1700K)$ of the oxidation reaction for the ten systems; (b) macroscopic appearance of the three systems after oxidation; (c, d) mass gain against time for TZH and THT at different temperatures; (e, f) squared mass gain against time; (g) Arrhenius plot of $k_p$ and (h) the corresponding residual analysis.

In Fig. 2(a) the abscissa is the $\Delta E_{\mathrm{form}}$ and the ordinate is the $\Delta G(1700K)$; the ranking does not change with temperature over the range 1000~1700 K. The formation energies of THT and ZHT are -1.44 and -1.41 eV/atom, respectively, compared with about -1.21 eV/atom for TZH, so that THT and ZHT appear thermodynamically more stable. In terms of the free energy of the oxidation reaction, TZH has the weakest driving force, whereas that of THT is clearly stronger than those of TZH and ZHT. On this basis ZHT performs well by both criteria and would therefore be expected to exhibit

Just Accepted

good oxidation resistance. It should be noted that TZH, THT and ZHT were not chosen as the best, second-best and worst systems, but as a representative set for testing the relationship between stability and oxidation resistance.

The results in Fig. 2(b) do not match the prediction in Fig. 2(a). ZHT, by contrast, failed much earlier: macroscopic cracks appeared at 1000 ℃ and the specimen had completely disintegrated into powder by 1200 ℃, so this system was excluded from the subsequent kinetic analysis. The mass-gain data in Fig. 2(c, d) reveal the difference between TZH and THT at high temperature. The mass gain per unit area increases with time for both systems, and the rate of gain rises with temperature: both gain little at 1200 ℃, whereas at 1400 ℃ the mass gain accumulates rapidly. At a given temperature and oxidation time, TZH always gains less than THT, indicating that both its oxidation reaction and the inward diffusion of oxygen into the substrate are suppressed more effectively.

The squared mass gain is plotted against time in Fig. 2(e, f); the data points are approximately linear, indicating that oxidation follows a parabolic law [55]. The activation energy reflects how sensitively the oxidation rate responds to temperature, that is, how readily the rate increases as the temperature rises [56,57]. To check whether a single activation energy is sufficient to describe the whole temperature range, $k_p$ was plotted in Arrhenius form (Fig. 2(g)). At all three temperatures the data points for THT lie above those for TZH, so that $k$p is consistently higher for THT. Over the full range, the activation energies of TZH and THT are 568.9 kJ/mol ($R^2$ = 0.949) and 512.3 kJ/mol ($R^2$ = 0.956), respectively, yet the temperature dependence does not follow a single Arrhenius line strictly. The residual plot in Fig. 2(h) is negative at both ends and positive in the middle, indicating that a single line underestimates $k_p$ at 1300 ℃ and overestimates it at the two end temperatures. Between 1200 and 1300 ℃ the activation energies of TZH and THT are 780.5 and 688.2 kJ/mol; between 1300 and 1400 ℃ they are 318.8 and 304.2 kJ/mol. This is consistent with the evolution of the oxide scale with temperature: at 1200~1300 ℃ the scale is relatively continuous and dense, oxygen is transported mainly through the oxide itself and short-circuit paths contribute little, whereas at 1300~1400 ℃ pores

Just Accepted

and cracks develop, the integrity of the scale decreases, the contribution of short-circuit paths grows, and the apparent activation energy falls markedly. It should be noted that, with only three temperatures ($n$ = 3), this interpretation is a plausible inference consistent with the observed defect development rather than a demonstration that the controlling step changes.

Taken together, ZHT shows the poorest oxidation resistance, whereas TZH and THT both perform well at 1000~1400 ℃, with TZH giving the lower kinetic response. These results are not consistent with the thermodynamic prediction: the thermodynamic stability of a carbide and the free energy of its oxidation reaction bear no simple correspondence to the oxidation resistance measured in practice, and thermodynamic parameters alone cannot serve as a criterion. Further descriptors are needed — the structure and defect evolution of the oxide scale, the oxygen adsorption energy and the oxygen penetration barrier [58]. The results presented below show that the superior oxidation resistance of TZH arises mainly from its stronger suppression of oxygen migration towards the subsurface, and from the relatively dense, continuous scale that this suppression produces.

### 3.2 Structural evolution and failure behavior of the oxide scale

To clarify the origin of the differences in oxidation resistance, the surface morphology, phase constitution and defect characteristics of the oxide scales are examined together in this section. TZH, THT and ZHT follow different modes of scale evolution during high-temperature oxidation, corresponding respectively to protection through densification, degradation through progressive porosity, and crack-dominated failure. These differences indicate that the continuity, density and defect state of the scale are the key factors governing whether oxidation remains suppressed.

Fig. 3 shows the macroscopic appearance of the three systems after isothermal oxidation. The extent of oxidation increases markedly with temperature and exposure time, and the surface colour changes from black through grey-white to beige, reflecting the progressive oxidation of the surface carbide and the transition to an oxide-dominated surface.

Just Accepted

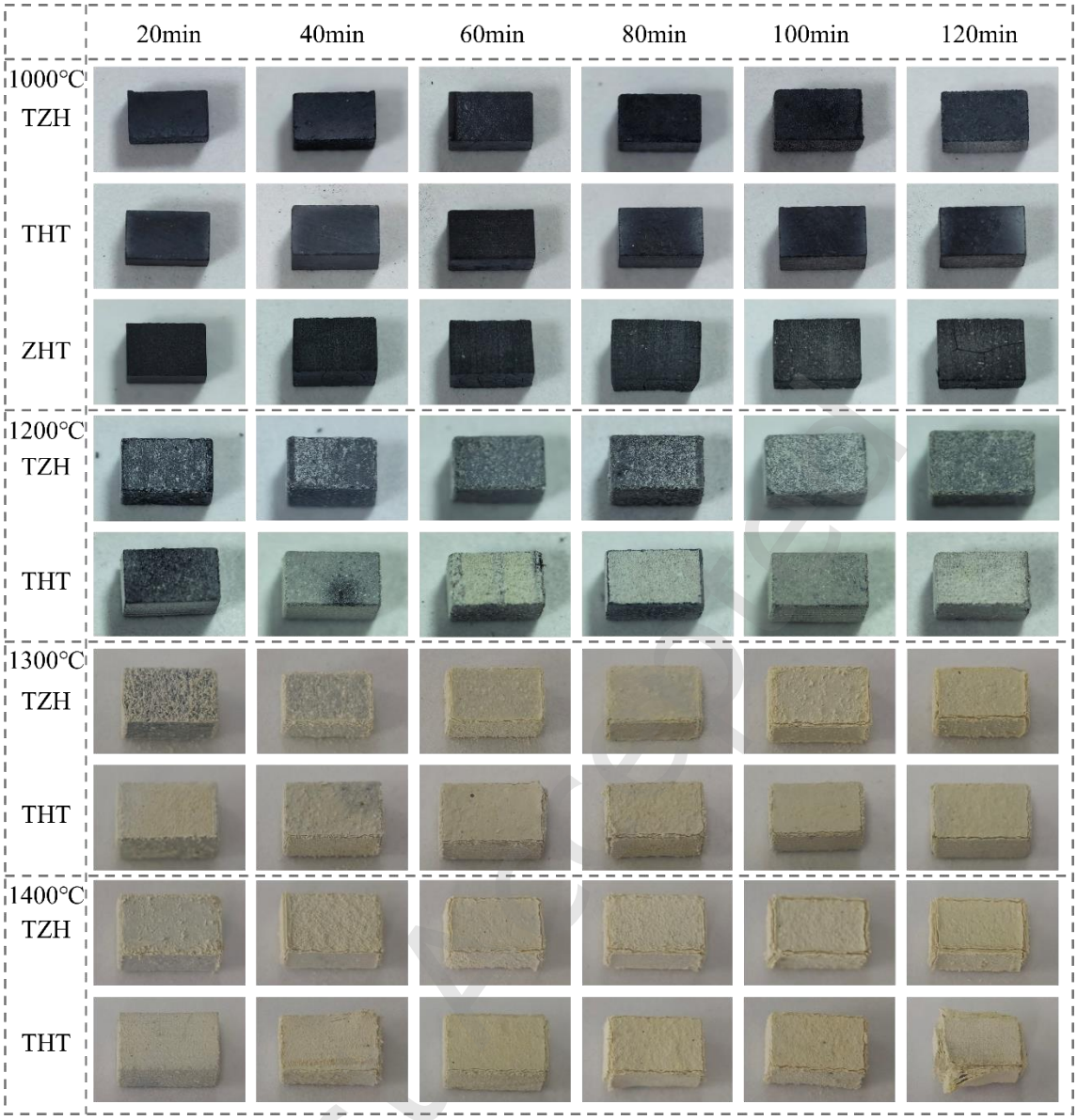



**Fig. 3** Macroscopic appearance of the three systems after oxidation at different temperatures and times.

Fig. 4(a–c) shows the XRD patterns and SEM images of TZH, THT and ZHT after oxidation. Oxide reflections appear in all three systems, and the oxide peaks become sharper as the temperature or the oxidation time increases. The XRD results indicate that a higher temperature mainly accelerates the formation and sintering of the oxide scale, and that no new oxide phases are detected. Peak sharpness is also affected by crystallinity, preferred orientation and instrumental broadening, so it is used here only as a qualitative indicator of grain growth and sintering, and not as a measure of the extent of oxidation.

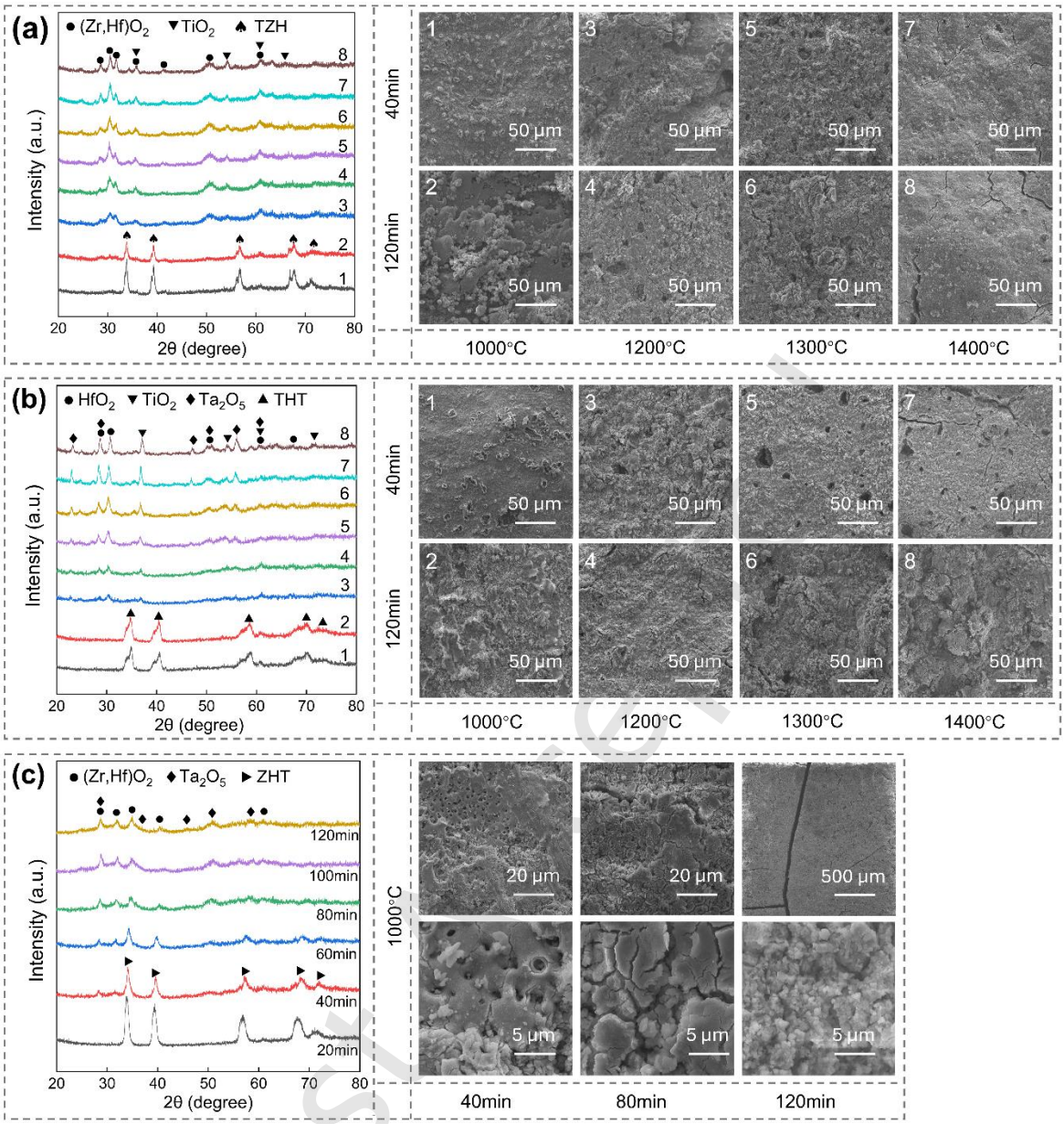



**Fig. 4** XRD patterns and surface SEM images of the three systems after oxidation under different conditions: (a) TZH, (b) THT, (c) ZHT.

The oxide scale on TZH consists mainly of $TiO_2$ (PDF#00-021-1276) and $(Zr,Hf)O_2$ (PDF#04-002-5428). In the early stage of oxidation the surface is covered with fine particulate oxide; as the exposure time and temperature increase, these particles sinter and gradually coalesce into a continuous layer, so that the scale shows a tendency towards densification. Between 1200 and 1400 ℃ a few micropores and fine cracks are visible on the TZH surface, but they are limited in number and do not develop into extensive through-thickness channels. The resulting continuous scale clearly impedes the inward

diffusion of oxygen under the conditions examined here, which is consistent with the lower mass gain of TZH. The scale on THT consists of several oxides, namely $TiO_2$, $HfO_2$ (PDF#00-034-0104) and $Ta_2O_5$ (PDF#00-025-0922). Its surface is covered fairly uniformly in the early stage, with relatively fine oxide particles and a scale of moderate density. As the temperature rises the scale thickens rapidly, and particle agglomeration, increasing porosity and local crack growth appear. The mismatch between the multiphase oxides, the volume change associated with the oxidation reaction, the accumulation of thermal stress and the pores left by $CO/CO_2$ evolution together drive the transition from a relatively dense scale at an early stage to a porous structure later on. The oxidation of ZHT is more clearly crack-dominated. ZHT oxidizes mainly to $(Zr,Hf)O_2$ and $Ta_2O_5$. At 1000 ℃ the surface evolves from small pits into a mud-crack network and then into wider through-thickness cracks. This crack network provides short-circuit paths that allow oxygen to reach the substrate quickly, so that oxidation keeps accelerating locally and the scale loses structural stability within a short time. ZHT therefore cracks and fails at a comparatively low oxidation temperature, and its failure mode differs from the progressive porosity of THT.

To quantify the surface defects of the oxide scales, Figs. S6 and S7 present the SEM images, binary images and crack skeletons of the two systems at different magnifications. The data extracted from these images are listed in Table S1 and visualized in Fig. 5.

Fig. 5(a–c) shows the surface defect area fraction $P_A$ at different temperatures and magnifications. Except at 1300 ℃ and 2000×, where $P_A$ of THT is lower than that of TZH, $P_A$ of THT exceeds that of TZH under all conditions. Overall, $P_A$ shows no clear increase with temperature, indicating that the oxide products undergo some sintering and densification during oxidation, a behaviour common to both systems. At 2000×, however, $P_A$ of THT rises from 7.96% at 1300 ℃ to 11.93% at 1400 ℃, suggesting that local cracking or spallation at high temperature creates more visible defects.

Fig. 5(d–f) shows the crack length density $L_A$. Between 1200 and 1300 ℃, $L_A$ of THT is higher than that of TZH at all magnifications, indicating a denser or longer crack network in the THT scale. At

Just Accepted

1400 °C, $L_A$ of TZH at 500× is 13.45 $mm^{-1}$, higher than the 10.32 $mm^{-1}$ of THT; at 1000× and 2000×, however, $L_A$ of THT is 21.42 and 43.34 $mm^{-1}$, still above the 18.44 and 35.54 $mm^{-1}$ of TZH. The local increase in $L_A$ of TZH at 500× therefore more likely reflects an inhomogeneous crack distribution and a limited field of view, and should not be taken as evidence that the overall crack damage in TZH exceeds that in THT.

Fig. 5(g–i) gives the length density of cracks ≥20 μm, $L_{A20}$. At 2000×, $L_{A20}$ of THT is higher than that of TZH at all temperatures, indicating a larger contribution from long cracks at high magnification. Notably, $L_A$ of THT at 1400 °C remains high while $L_{A20}$ decreases, showing that the total crack length at this temperature is dominated by numerous fine cracks rather than by a few very long ones. For TZH, $L_{A20}$ at 1400 °C is 5.88 and 6.66 $mm^{-1}$ at 500× and 1000×, higher than the corresponding values at 1200 and 1300 °C, which suggests a local transition from a fine-crack network to a few longer cracks; the constraint exerted by pores on crack propagation weakens, and growth stress together with cooling-induced thermal mismatch becomes dominant. No cracks ≥20 μm were detected at 2000×, possibly because of the limited field of view. Cracks in TZH at 1400 °C do not disappear; rather, the overall defect area remains low while longer cracks exist locally.

Just Accepted

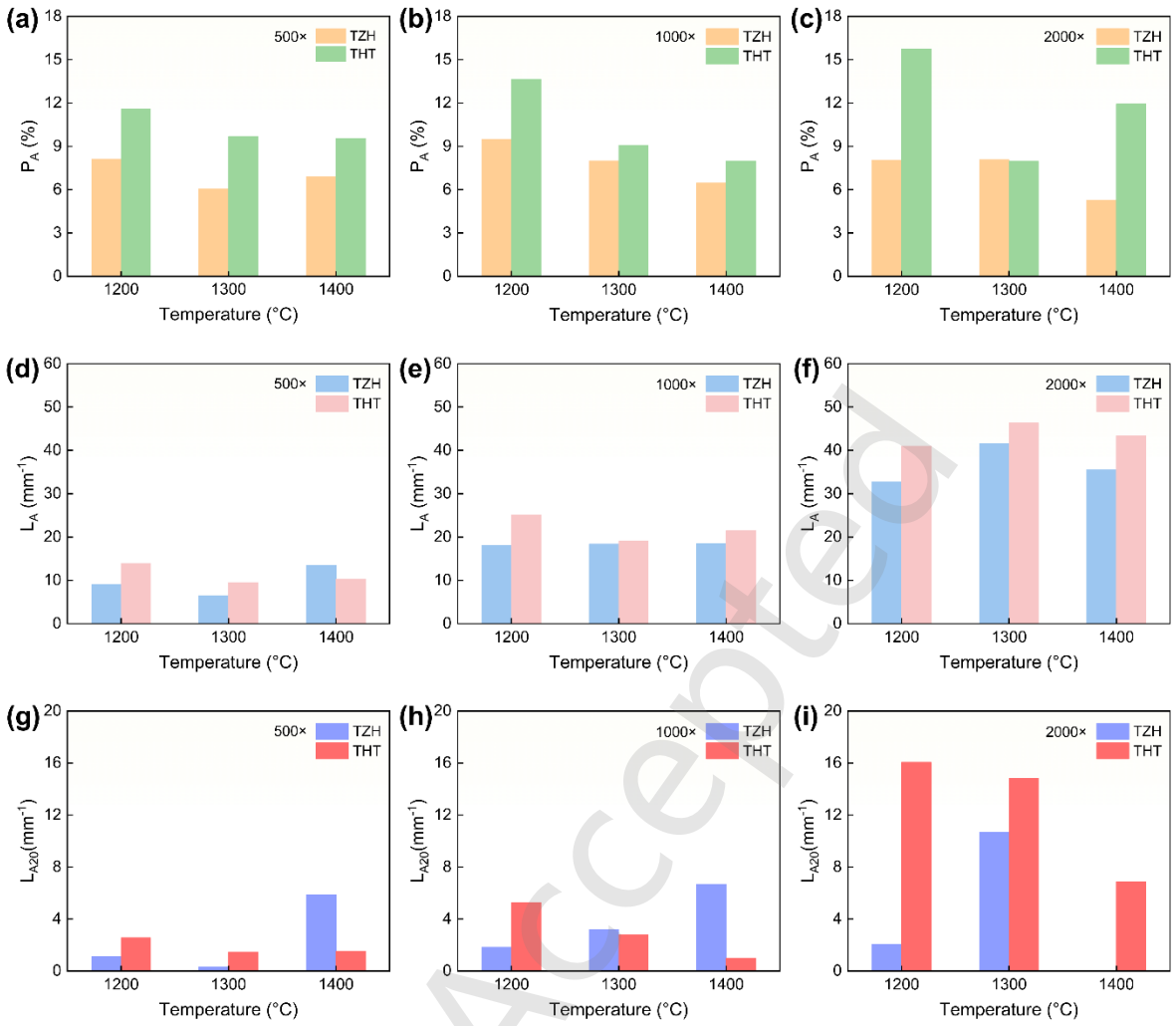



**Fig. 5** Damage statistics for the surface oxide scales of TZH and THT: (a–c) surface defect area fraction, (d–f) crack length density, (g–i) length density of cracks ≥20 μm. In each group, the three panels correspond to 500×, 1000× and 2000× magnification, respectively.

Overall, TZH shows a lower surface defect area fraction under most conditions, together with a lower crack length density and a smaller long-crack contribution at 1200~1300 °C, indicating that its scale is more continuous and offers fewer surface paths for oxygen transport. THT shows a higher defect area fraction and a denser crack network, indicating a greater tendency towards defect accumulation and local instability. These results agree with the morphological observations in Fig. 4 and Figs. S6 and S7, and provide quantitative support for the assessment of scale integrity.

Just Accepted

Beyond phase composition and morphology, the three systems share a common feature during oxidation: carbon escapes as CO and $CO_2$ [59,60]. On the basis of the oxidation products identified by XRD, the idealised oxidation reactions of the constituent carbides can be written as:

$$MC + \frac{3}{2}O_2 \rightarrow MO_2 + CO \quad (M = Ti,\ Zr,\ Hf)$$

$$TaC + \frac{7}{4}O_2 \rightarrow \frac{1}{2}Ta_2O_5 + CO$$

Whatever the actual $CO/CO_2$ ratio, each mole of carbide formula units contains one carbon atom and therefore releases 1 mol of carbon-bearing gas. The mass gain of the solid phase is set by the oxygen incorporated into the oxide, and not by whether the carbon leaves as CO or as $CO_2$. Using CO as the representative carbon-bearing gas in the stoichiometric analysis therefore does not alter the mass balance of the solid phase. Taking the molar volume of a gas under standard conditions, the theoretical amount of carbon-bearing gas generated per unit initial volume is approximately $1.57\times10^3$, $1.66\times10^3$ and $1.53\times10^3$ for TZH, THT and ZHT, respectively — values that fall within a narrow range, indicating that gas evolution is a pore-forming factor common to the oxidation of all three materials.

The Pilling–Bedworth ratio (PBR) can be used to describe, semi-quantitatively, the volume change of the solid phase caused by oxidation and its effect on the integrity of the oxide scale; the results are shown in Fig. 6(a). In general, a PBR of about 1–2 favors the formation of a relatively continuous scale, whereas a PBR above 2 implies that the volume expansion of the oxidation products may accumulate appreciable compressive stress and thereby increase the tendency towards cracking and spallation. The high PBR associated with the formation of $Ta_2O_5$ from TaC therefore indicates a stronger driving force for volume expansion in this reaction [61]. For the multi-component carbides, the total oxide volume was weighted against the total carbide volume according to the stoichiometry of the individual reactions [62,63], giving equivalent PBRs of 1.42, 1.64 and 1.57 for TZH, THT and ZHT and equivalent linear strains of approximately 12.4%, 18.0% and 16.2%. The Ta-containing

Just Accepted

systems therefore undergo a larger oxidation-induced volume change and are, in principle, more prone to local compressive stress, porosity and cracking.

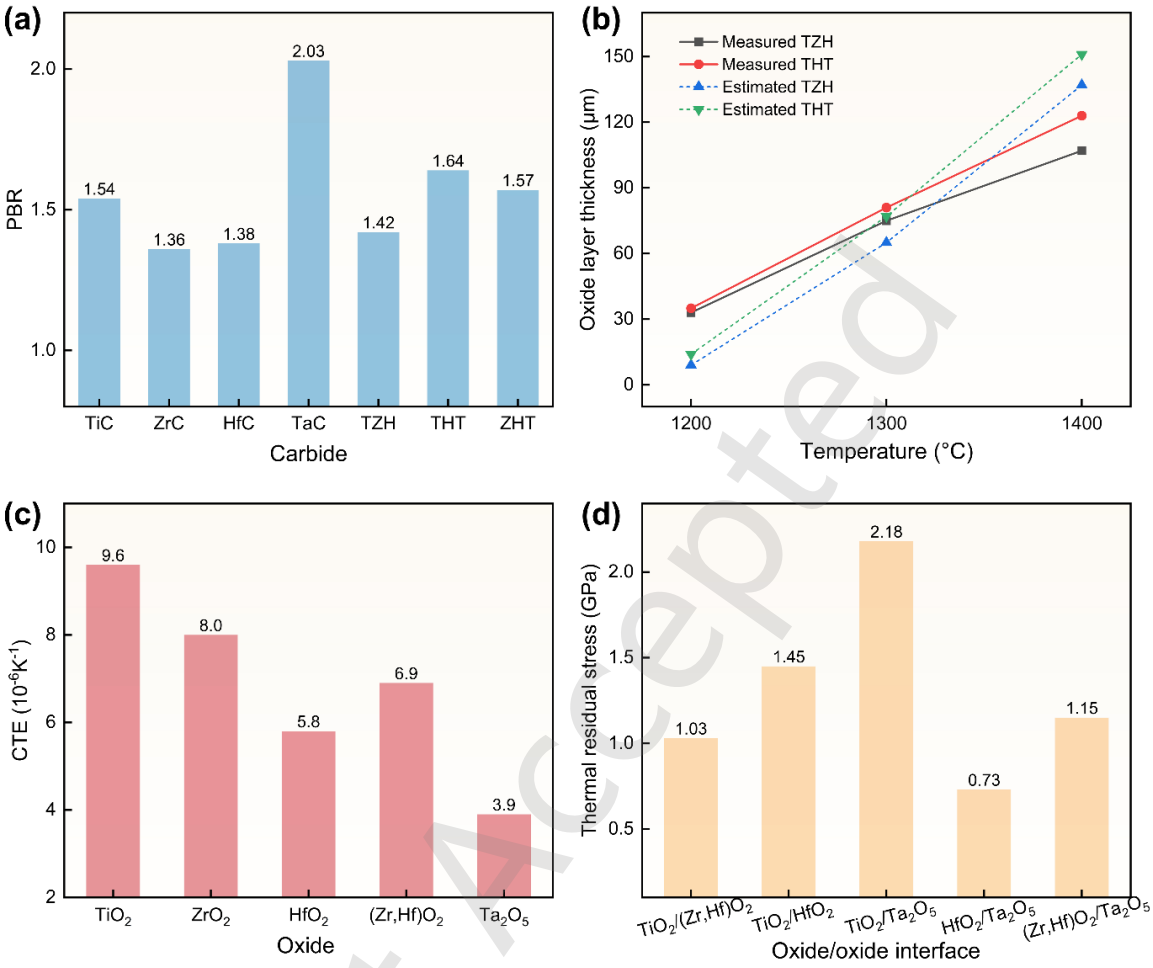



**Fig. 6** Thermophysical criteria for the growth and integrity of the oxide scale: (a) PBR of the constituent binary carbides and of the MECs; (b) estimated and measured oxide-scale thickness; (c) thermal expansion coefficients of the constituent oxides; (d) thermal stress at different oxide/oxide interfaces.

To test the consistency between the stoichiometric analysis and the measured oxidation kinetics, the theoretical mass gain per unit initial volume was calculated for the three materials, giving 1.40, 1.68 and 1.55 g/cm$^3$ for TZH, THT and ZHT, respectively. From the ΔW/A data in Fig. 2(c, d), the values at 1200, 1300 and 1400 ℃ are 1.154 and 1.923, 8.077 and 11.025, and 17.025 and 21.436 mg·cm$^{-2}$ for TZH and THT, corresponding to THT/TZH ratios of 1.67, 1.36 and 1.26. As the temperature rises, this ratio approaches the theoretical mass-gain ratio of 1.68/1.40 ≈ 1.2. On the basis of the ΔW/A values and the equivalent PBR, the thickness of the oxide scale was further estimated at each temperature

Just Accepted

(Fig. 6(b)). The estimated values are of the same order of magnitude as those measured on cross-sections by SEM (Fig. S8), and both increase with temperature.

The thermal expansion coefficients of the oxides and the thermal mismatch at their interfaces were examined next. The coefficients of the oxides listed in Fig. 6(c) range from about 3.9~9.6×$10^{-6}$ $K^{-1}$, and the mismatch between different oxides from about 1.9~5.7×$10^{-6}$ $K^{-1}$ [64–67]. Under the idealized conditions of fully elastic constraint, with creep and plastic deformation neglected, the thermal stress is estimated to be 0.73~2.18 GPa (Fig. 6(d)). Thermal expansion mismatch can therefore provide a driving force large enough to initiate cracks, particularly at multiphase interfaces where the difference in thermal expansion is greatest. Because a real scale relieves part of this stress through microcracking, porosity and interfacial sliding, the values in Fig. 6(d) should be read as an upper estimate for ideal elastic constraint rather than as experimentally measured stresses.

Taken together, the three systems follow different modes of scale evolution. The scale on TZH has a low surface defect area fraction and a low crack length density; its oxidation products continue to sinter and remain relatively continuous, which corresponds to protection through densification. THT has a higher equivalent PBR, a higher pore fraction and a higher crack density, and gas evolution together with thermal mismatch at the multiphase interfaces drives the progressive loosening and local cracking of its scale. ZHT does not experience the highest theoretical thermal stress, yet the mud-crack network formed early in oxidation connects rapidly, so that oxygen diffuses along short-circuit paths and the scale fails. Overall, carbon-bearing gas evolution is a pore-forming factor common to all three systems, PBR and thermal expansion mismatch supply the driving force for defect formation, and it is the propagation and connectivity of cracks that determine the final oxidation behavior.

### 3.3 Oxygen adsorption at the surface and penetration into the subsurface

To describe the initial step of oxygen entering the carbide lattice at the atomic scale, oxygen adsorption on the (111) surfaces of TZH, THT and ZHT and its migration from the surface to subsurface interstitial sites were calculated [68–71].

Just Accepted

**Table 1** Calculated oxygen adsorption energies for the three systems.

| Sample | $E_{slab}$ (eV) | $E_{surf+O}$ (eV) | $E_{inter+O}$ (eV) | $E_{ads,surf}$ (eV) | $E_{ads,inter}$ (eV) | ΔE (eV) |
|---|---|---|---|---|---|---|
| (TiZrHf)C | -444.413 | -455.851 | -449.924 | -6.612 | -0.685 | 5.927 |
| (TiHfTa)C | -467.754 | -478.428 | -473.706 | -5.848 | -1.126 | 4.722 |
| (ZrHfTa)C | -471.799 | -483.818 | -478.494 | -7.193 | -1.869 | 5.324 |

Table 1 shows that $E_{\mathrm{ads,surf}}$ is -6.612, -5.848 and -7.193 eV for TZH, THT and ZHT, respectively, so all three systems exhibit a strong tendency to adsorb oxygen. The differences between them arise mainly from the local chemical environment of the metal atoms around the adsorption site: ZHT has the most negative adsorption energy, indicating that the coordination environment formed by Zr, Hf and Ta captures oxygen most strongly; TZH follows, and THT is the weakest. ZHT has the strongest $E_{\mathrm{ads,surf}}$ and should therefore capture oxygen and nucleate oxide most readily, yet it fails most completely, which shows that the tendency to nucleate is decoupled from the ability to protect. Surface adsorption appears to be only the first step of oxidation; it is the penetration of oxygen into the interior that governs performance during sustained oxidation. For all systems the magnitude of $E_{ads,inter}$ is below 2 eV, far smaller than that of $E_{\mathrm{ads,surf}}$, indicating that oxygen is only weakly stabilised at interstitial sites. TZH has the weakest $E_{ads,inter}$, so its interstitial environment binds oxygen least strongly, and oxygen that enters is driven back to the surface by a strong "repulsive" force. In ZHT and THT, $E_{ads,inter}$ is somewhat more negative and the binding is stronger than in TZH, which may provide a route for oxygen to accumulate gradually within the material during oxidation.

$\Delta E$ is the difference between $E_{ads,inter}$ and $E_{\mathrm{ads,surf}}$, and represents the thermodynamic energy cost of transferring oxygen from a surface adsorption site to an interstitial site. $\Delta E$ is +5.927 eV for TZH, higher than the +5.324 eV of ZHT and the +4.722 eV of THT. Even without considering the transition-state barrier along the migration path, transferring oxygen from the surface to the interstitial site at equilibrium therefore requires almost 6 eV. Taking a Boltzmann distribution at 1673 K,

For TZH：

Just Accepted

$$\frac{N_{inter}}{N_{surf}} = \exp\left(-\frac{\Delta E}{k_B T}\right) = \exp\left(-\frac{5.927}{0.144}\right) \approx 10^{-18}$$

For THT：

$$\frac{N_{inter}}{N_{surf}} = \exp\left(-\frac{\Delta E}{k_B T}\right) = \exp\left(-\frac{4.722}{0.144}\right) \approx 10^{-15}$$

This means that, even at thermal equilibrium, the occupation probability of oxygen at interstitial sites in TZH is only $10^{-18}$ of that at the surface, so oxygen is thermodynamically favoured to remain at the surface. Under the same conditions the corresponding value for THT is $10^{-15}$, much higher than that for TZH.

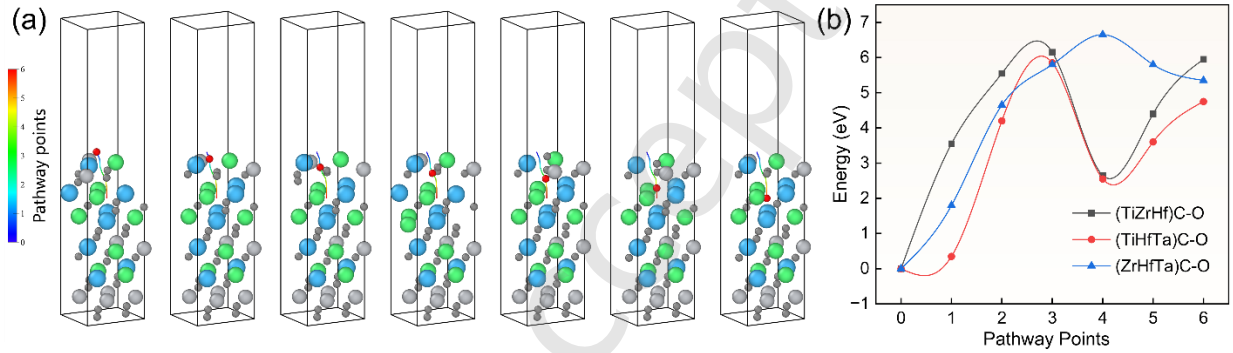



**Fig. 7** (a) The climbing-image nudged elastic band (CI-NEB) method and (b) energy profiles calculated with CI-NEB for oxygen migration in the three systems.

The transition-state barrier for oxygen migration from a surface adsorption site to a subsurface interstitial site was then calculated with the climbing-image nudged elastic band (CI-NEB) method [72], as shown in Fig. 7. The surface-to-subsurface penetration barriers of TZH, THT and ZHT are 6.3, 6.0 and 6.7 eV, respectively, indicating that oxygen migration from the surface to the subsurface is energetically very demanding. This is consistent with the thermodynamic preference of oxygen to remain at the surface described above. In all three systems the relative energy at the end of the path remains high, with the final state lying well above the initial state, which confirms the positive $\Delta E$. Even if oxygen overcomes the kinetic barrier and enters the subsurface, a strong thermodynamic driving force therefore acts to return it to the surface.

Just Accepted

Among the three systems, TZH shows the best oxidation resistance: its $E_{ads,inter}$ is the weakest (-0.685 eV) and the final state of its NEB profile is the highest (~6.0 eV), only 0.3 eV below the transition-state peak (~6.3 eV). Oxygen that crosses the barrier into the interstitial site therefore gains no stabilisation at all and is rapidly driven back to the surface. The weak binding at the interstitial site thus produces a combined thermodynamic and kinetic barrier in the initial oxidation step, which provides an atomic-scale basis for the stronger suppression of oxygen penetration in TZH during early oxidation. In ZHT the migration barrier is the highest (~6.7 eV), consistent with its strongest $E_{ads,surf}$ (-7.193 eV), but $E_{ads,inter}$ is relatively high (-1.869 eV) and the final state falls back considerably (~5.4 eV), indicating that the interstitial environment still binds oxygen to some extent. THT has both the lowest migration barrier (~6.0 eV) and the lowest final-state energy (~4.7 eV), consistent with its weakest $E_{ads,surf}$ (-5.848 eV); its combined barrier is therefore the weakest of the three.

Accordingly, the oxidation process is treated here as two linked stages comprising four processes in total. The first stage is the initial step by which oxygen enters the carbide lattice, that is, process 1, in which oxygen passes from the carbide surface into a subsurface interstitial site, described by the surface adsorption energy and the surface-to-subsurface penetration barrier; the calculations in this section address precisely this stage. The second stage is the formation, evolution and failure of the oxide scale, which can be resolved into three processes: process 2, transport of oxygen through the oxide lattice, whose temperature dependence is reflected in the apparent activation energy derived from the parabolic rate constant (Section 3.1); process 3, crossing of oxygen across oxide/oxide and oxide/carbide interfaces, whose driving force is given by the PBR and the thermal expansion mismatch (Section 3.2); and process 4, short-circuit transport of oxygen along cracks and pores, reflected jointly by the surface defect statistics and by the oxidation kinetics (Section 3.2). The two stages are linked: the first sets the tendency for oxygen ingress during early oxidation and hence influences how rapidly and how densely the early scale forms; once the scale has formed, subsequent oxygen transport passes to the second stage and comes under the control of the scale continuity, density and defect connectivity.

Just Accepted

The atomistic calculations therefore indicate the tendency for oxygen ingress at the initial stage, whereas the scale microstructure observed experimentally determines whether that suppression can be maintained during continued oxidation.

It should be noted that the present work does not describe the growth of the oxide scale at the atomic scale. A complete description would require calculations of oxygen transport through the lattice and along grain boundaries in $TiO_2$, $ZrO_2/HfO_2$ and $Ta_2O_5$, and of oxygen crossing the carbide/oxide interfaces; these lie beyond the scope of this study and are left for future work.

### 3.4 Analysis of oxidation resistance mechanisms

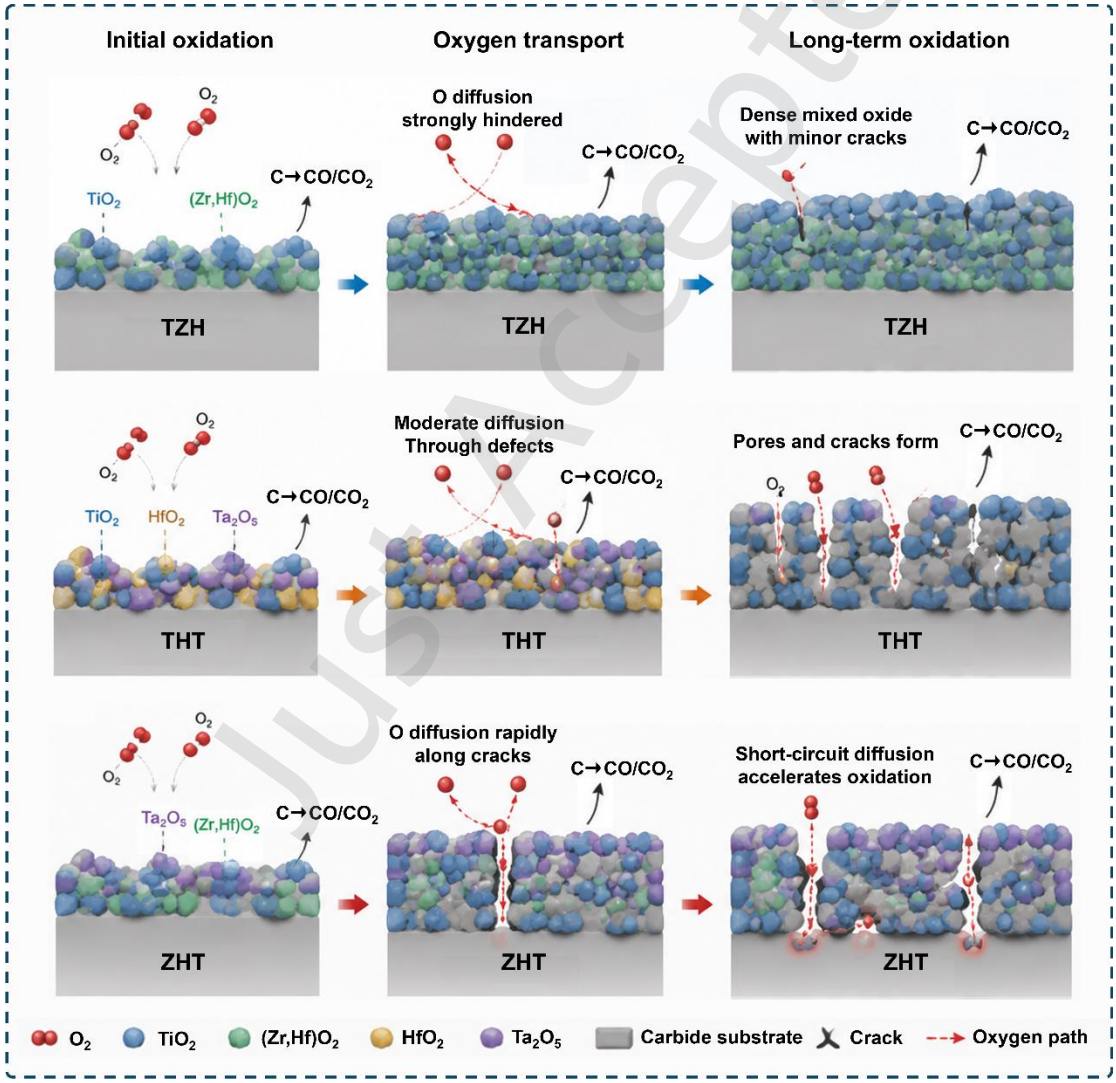



**Fig. 8** Schematic of the oxidation process proposed for the three systems: (a) TZH, (b) THT, (c) ZHT.

Just Accepted

Drawing on the observed changes in macroscopic appearance, phase analysis, microstructural characterization, oxidation kinetics and first-principles calculations, the three MECs are shown to differ markedly in their oxidation behavior and failure modes at high temperature. Fig. 8 summarizes the oxidation mechanism proposed for each system.

As shown in Fig. 8(a), TZH exhibits the best oxidation resistance under the conditions examined, 1000~1400 ℃ for up to 120 min. Its mechanism can be understood as a synergy of "strong surface adsorption and suppressed subsurface penetration": the surface adsorption energy is -6.612 eV while the interstitial site gives only -0.685 eV, and $\Delta E$ = 5.927 eV constitutes a substantial energy barrier that "pins" oxygen at the surface. In the early stage Ti, Zr and Hf oxidise to $TiO_2$ and $(Zr,Hf)O_2$, while C escapes as CO and $CO_2$. With increasing temperature and time the oxides grow and sinter, the scale becomes continuous and dense, and the oxidation kinetics follow a parabolic law between 20 and 120 min. After oxidation at 1400 ℃ for 120 min, thermal stress generates a crack network, yet the scale still covers the surface continuously and adheres well to the substrate, with no large-area spallation; within the conditions and time window of this study the scale on TZH therefore retains good integrity. Its intrinsic suppression of oxygen entry (the high $\Delta E$), together with the continuity and density of the scale, accounts for its better performance than THT.

As shown in Fig. 8(b), THT undergoes a transition from early dense protection to later porous degradation. Its surface adsorption energy is -5.848 eV and its interstitial energy -1.126 eV, giving $\Delta E$ = 4.722 eV, lower than that of TZH, so that oxygen more readily breaks through the surface-to-subsurface barrier. In the early stage Ti, Hf and Ta oxidize together to form a mixed layer of $TiO_2$, $HfO_2$ and $Ta_2O_5$. As the temperature and time increase, thermal mismatch stress is released at defects and initiates and propagates cracks, interlayer porosity grows, and the porous scale loses its barrier capability. This dense-to-porous transition markedly reduces the oxidation resistance of THT at higher temperatures, and the scale gradually ceases to protect the substrate.

Just Accepted

As shown in Fig. 8(c), ZHT undergoes cracking-dominated failure in which short-circuit diffusion prevails. Its surface adsorption energy is as high as -7.193 eV, but the interstitial energy reaches -1.869 eV, indicating that once oxygen crosses the barrier it is relatively stable in the subsurface; its subsequent long-range transport to the substrate is then controlled by short-circuit channels formed by cracks and pores. Volume expansion of the oxides and thermal mismatch stress act together, so that microcracks form early in oxidation and grow into macroscopic through-thickness cracks. $O_2$ then diffuses along these cracks directly to the substrate, triggering a new round of rapid oxidation.

## 4 Conclusions

This work addresses the selection of MECs and the failure of single thermodynamic indicators to predict their behavior, and establishes a framework of thermodynamic screening, experimental validation and mechanistic analysis. The main conclusions are as follows.

(1) A single thermodynamic indicator cannot predict the oxidation resistance of MECs reliably. TZH has the least negative average atomic formation energy (the lowest thermodynamic stability), yet offers the best protection, whereas ZHT fails completely through severe cracking. Formation energy or the driving force for oxidation is therefore not sufficient on its own as a criterion, and a more integrated assessment is required.

(2) The inward diffusion kinetics of oxygen and the structural integrity of the oxide scale together determine the oxidation behavior. The atomic-scale adsorption energy and penetration barrier set the tendency for oxygen to enter the carbide lattice in the early stage; once the scale has formed, its continuity, density and defect connectivity take control of oxygen transport and can amplify or reverse that initial tendency. Short-circuit channels formed by pores and through-thickness cracks are the clearest expression of the latter. Experimentally, the scale on TZH sinters fully and becomes dense, with thermal-stress-induced microcracks as its main defect, and provides the best protection; the scale on THT is porous and contains voids, so oxygen can diffuse inward along defects; and ZHT fails rapidly because its scale cracks severely.

Just Accepted

(3) Under the conditions examined here, the better oxidation resistance of TZH arises from a synergy of strong surface adsorption, suppressed penetration and a dense scale: the larger $\Delta E$ lowers the tendency for oxygen to pass from the surface into the subsurface, and the continuous, dense scale limits its subsequent transport, so that protection operates at both the atomic and the mesoscale.

These results argue for replacing single-criterion thermodynamic screening with a combined framework that couples oxygen transport kinetics to scale structure, and provide a basis for the targeted design of MECs in aerospace thermal protection.

**Acknowledgements**

The authors acknowledge the financial support of National Natural Science Foundation of China (U2241239) and Science and Technology Innovation Program of Hunan Province (2023RC3024).

**Funding**

The authors acknowledge the financial support of National Natural Science Foundation of China (U2241239) and Science and Technology Innovation Program of Hunan Province (2023RC3024).

**Author contributions**

Chenyi Xie: Writing – review & editing, Writing – original draft, Formal analysis, Data curation.

Huaming Miao: Writing – review & editing, Formal analysis, Data curation.

Weiran Zhang: Formal analysis, Data curation.

Yanfei Wang: Writing – review & editing, Project administration, Funding acquisition.

Duan Li: Writing – review & editing, Project administration, Funding acquisition.

Rongjun Liu: Writing – review & editing, Project administration, Funding acquisition.

Just Accepted

**Availability of data and materials**

The data that support the findings of this study are available from the corresponding author upon reasonable request."

**Competing interests**

The authors have no competing interests to declare that are relevant to the content of this article.

**Electronic Supplementary Material (ESM)**

Electronic Supplementary Material: Supplementary material is available in the online version of this article.

**References**

[1] Peters AB, Zhang D, Chen S, *et al.* Materials design for hypersonics. *Nat Commun* 2024, **15**: 3328.

[2] Gülhan A, Hargarten D, Zurkaulen M, *et al.* Selected results of the hypersonic flight experiment STORT. *Acta Astronaut* 2023, **211**: 333–343.

[3] Shojaie-bahaabad M, Bozorg M, Najafizadeh M, *et al.* Ultra high temperature ceramic coatings in thermal protection systems (TPS). *Ceram Int* 2024, **50**: 9937–9951.

[4] Padture NP. Advanced structural ceramics in aerospace propulsion. *Nat Mater* 2016, **15**: 804–809.

[5] Al-Jothery HKM, Albarody TMB, Yusoff PSM, *et al.* A review of ultra-high temperature materials for thermal protection system. *IOP Conf Ser Mater Sci Eng* 2020, **863**: 012003.

[6] Binner J, Porter M, Baker B, *et al.* Selection, processing, properties and applications of ultra-high temperature ceramic matrix composites, UHTCMCs–a review. *Inter Mater Rev* 2020, **65**: 389–444.

[7] Hu F, Wang J, Sui Z, *et al.* A review on research progress of large area thermal protection structures for hypersonic vehicles. *Acta Astronaut* 2025, **232**: 541–556.

Just Accepted

[8] Li X, Fu Q, Wen Z, *et al.* Research Progress on Ultra-high Temperature Ceramic Structural Materials for Extreme Environments. *J Inorg Mater* 2025, **40**: 1045–1078.

[9] Zhang X, Wang Y, Cheng Y, *et al.* Research Progress on Ultra-high Temperature Ceramic Composites. *J Inorg Mater* 2024, **39**: 571–590.

[10] Jin G, Liang B, Zhao R, *et al.* Exceptional long-duration ablation tolerance over 2500℃ of C/ZrC-SiC-$Cu_3Si$-Cu interpenetrating composites. *J Adv Ceram* 2026, **15:** 9221334.

[11] Rubio V, Binner J, Cousinet S, *et al.* Materials characteriation and mechanical properties of $C_f$-UHTC powder composites. *J Eur Ceram Soc* 2019, **39**: 813–824.

[12] Tang S, Hu C. Design, Preparation and Properties of Carbon Fiber Reinforced Ultra-High Temperature Ceramic Composites for Aerospace Applications: A Review. *J Mater Sci Technol* 2017, **33**: 117–130.

[13] Arai Y, Inoue R, Goto K, *et al.* Carbon fiber reinforced ultra-high temperature ceramic matrix composites: A review. *Ceram Int* 2019, **45**: 14481–14489.

[14] Zhu T, Wang Z. Advances in processing and ablation properties of carbon fiber reinforced ultra-high temperature ceramic composites. *Rev Adv Mater Sci* 2024, **63**: 20240029.

[15] Wang Y, Xu J, Chen B, *et al.* Distinct lattice distortion role in high entropy diboride ceramics. *Mater Today* 2025, **92**: 115-125.

[16] Xie C, Miao H, Zhang W, *et al.* Research Progress of Theoretical Calculation in the Field of High-entropy Ceramics. *J Inorg Mater* 2026, **41**: 545-560.

[17] Hsu WL, Tsai CW, Yeh AC, *et al.* Clarifying the four core effects of high-entropy materials. *Nat Rev Chem* 2024, **8**: 471–485.

[18] Shao Z, Wu Z, Sun L, *et al.* High entropy ultra-high temperature ceramic thermal insulator $(Zr_{1/5}Hf_{1/5}Nb_{1/5}Ta_{1/5}Ti_{1/5})C$ with controlled microstructure and outstanding properties. *J Mater Sci Technol* 2022, **119**: 190–199.

Just Accepted

[19] Wang H, Wang S, Cao Y, *et al.* Oxidation behaviors of $(Hf_{0.25}Zr_{0.25}Ta_{0.25}Nb_{0.25})C$ and $(Hf_{0.25}Zr_{0.25}Ta_{0.25}Nb_{0.25})C$-SiC at 1300–1500 ℃. *J Mater Sci Technol* 2021, **60**: 147–155.

[20] Wang K, Chen L, Xu C, *et al.* Microstructure and mechanical properties of (TiZrNbTaMo)C high-entropy ceramic. *J Mater Sci Technol* 2020, **39**: 99–105.

[21] Liu L, Yang W, Mo J, *et al.* Microstructure and mechanical properties of novel medium-entropy carbide ceramics. *Comput Mater Sci* 2023, **230**: 112464.

[22] Zhang X, Yang X, Luo X, *et al.* Formation mechanism of (Ti, Zr, Hf)C medium-entropy carbide derived from polymer precursors and its modification on the ablative mechanism of C/C-SiC composites. *Corros Sci* 2024, **230**: 111935.

[23] Zhang Z, Hou C, Zhang Z, *et al.* Data-Driven Design of Spinodal Decomposition in (Ti, Zr, Hf)C Composite Carbides for Optimizing the Hardness-Toughness Trade-Off. *Adv Funct Mater* 2025, **35**: 2502555.

[24] Xu J, Sun W, Xiong X, *et al.* C/C-$(Hf_{0.5}Zr_{0.3}Ti_{0.2})C$–W–Cu composites: Long-term ablation resistance based on active-passive protection at 2600 ℃. *Compos B Eng* 2025, **289**: 111889.

[25] Gao S, Wang Y, Hu J, *et al.* Ablation behaviour of multi-component (Hf, Zr, Ti)C ceramics modified carbon/carbon composites. *J Eur Ceram Soc* 2025, **45**: 117141.

[26] Song X, Yan H, Cui T, *et al.* Ablation behavior of medium entropy carbide ceramics with different molar ratios of (Hf, Zr, Ti)C in oxyacetylene flame. *Ceram Int* 2025, **51**: 5987–5997.

[27] Li J, Zhang Y, Zhao Y, *et al.* A novel $(Hf_{1/3}Zr_{1/3}Ti_{1/3})C$ medium-entropy carbide coating with excellent long-life ablation resistance applied above 2100 ℃. *Compos B Eng* 2023, **251**: 110467.

[28] Jin C, Xiong K, Guo L, *et al.* A DFT insight into the mechanical, electronic and thermodynamic properties of (TiZrHf)C medium-entropy carbide ceramic. *Results Phys* 2022, **35**: 105341.

[29] Lu L, Wang S, Jiang T, *et al.* Nature-inspired (Ti,Zr,Hf)C/SiC micro-nano composites with enhanced ablation resistance through a Gobi Desert-like protective oxide layer. *J Adv Ceram* 2025, **14**: 9221151.

Just Accepted

[30] Fu F, Zhang W, Chen Z, *et al.* Effect of varying carbon content on microstructural evolution and mechanical properties of (TiZrHf)$C_x$–Ni cermets. *J Am Ceram Soc* 2025, **108:** e70134.

[31] Filipović S, Fahrenholtz WG, Hilmas GE, *et al.* Synergystic properties of dual phase (Hf,Ti,Zr)$B_2$–(Hf,Ti,Zr)C ceramics. *J Eur Ceram Soc* 2025, **45:** 117448.

[32] Lu L, Wen Q, Hu J, *et al.* Single-source-precursor synthesis and air-plasma ablation behavior of (Ti, Zr, Hf)C/SiC ceramic nanocomposites at 2200 ℃. *J Adv Ceram* 2024, **13**: 1043–1059.

[33] Lun H, Zeng Y, Xiong X, *et al.* Oxidation behavior of non-stoichiometric (Zr,Hf,Ti)$C_x$ carbide solid solution powders in air. *J Adv Ceram* 2021, **10**: 741–757.

[34] Song X, Zhang Z, Ye L, *et al.* Preparation and ablation behavior analysis of non-equimolar $C_f$/($Hf_{1/2}Zr_{1/3}Ti_{1/6}$)C composites under oxyacetylene flame with different heat fluxes. *Ceram Int* 2024, **50**: 26482–26492.

[35] Guo W, Gong J, Zhu L, *et al.* Oxidation and ablation resistance of (TiZrHf)C medium-entropy ceramic coating on C/C composite constructed in-situ at low temperature down to 900 ℃. *J Eur Ceram Soc* 2025, **45**: 116976.

[36] Chen S, Wang J, Chen Z, *et al.* Nb- and Ta-doped (Hf,Zr,Ti)C multicomponent carbides with enhanced oxidation resistance at 2500 ℃. *J Adv Ceram* 2024, **13**: 332–344.

[37] Li F, Zheng L, Liu Z, *et al.* Insight into the evolution mechanism and properties of SiC modified (Ti, Zr, Hf)C multi-phase ceramics synthesized via the sol-gel method. *J Eur Ceram Soc* 2025, **45**: 117619.

[38] Yan S, Song X, Yan H, *et al.* Influence of curing atmosphere on the pyrolysis mechanism of ($Hf_{1/2}Zr_{1/3}Ti_{1/6}$)C precursor. *J Am Ceram Soc* 2025, **108**: e70023.

[39] Wang XF, Wang XG, Yang QQ, *et al.* High-strength medium-entropy (Ti,Zr,Hf)C ceramics up to 1800 ℃. *J Am Ceram Soc* 2021, **104**: 2436–2441.

[40] Yang QQ, Wang XG, Wu P, *et al.* Ultra-high strength medium-entropy (Ti,Zr,Ta)C ceramics at 1800℃ by consolidating a core-shell structured powder. *J Am Ceram Soc* 2022, **105**: 823–829.

Just Accepted

[41] Demirskyi D, Nishimura T, Suzuki TS, *et al.* High-temperature toughening in ternary medium-entropy $(Ta_{1/3}Ti_{1/3}Zr_{1/3})C$ carbide consolidated using spark-plasma sintering. *J Asian Ceram Soc* 2020, **8**: 1262–1270.

[42] Xiong K, You L, Zhang S, *et al.* Pressure and temperature effects on (TiZrTa)C medium-entropy carbide from first-principles. *J Mater Res Technol* 2023, **23**: 2288–2300.

[43] Wang L, Cao X, Li Z, *et al.* Synthesis and oxidation behavior of Ti-Zr-Ta(Hf) high entropy carbide nanopowders by sol-gel method. *Ceram Int* 2024, **50**: 52439–52450.

[44] Li X, Hu D, Fu J, *et al.* Insights into (Hf-Zr-Ta-Nb)C thermal protective system: Ablation behavior, morphology evolution and atomic bonding. *Ceram Int* 2024, **50**: 12557–12565.

[45] Suvorova V, Suvorov D, Volodko S, *et al.* High-entropy carbonitrides with superior oxidation resistance: Fabrication and investigation of oxidation behavior under non-isothermal and isothermal conditions. *J Eur Ceram Soc* 2025, **45**: 116980.

[46] Yi G, Kuang J, Zou G, *et al.* Enhanced high-temperature oxidation resistance of compositionally optimized medium-entropy carbide $(Hf_{1/3}Ta_{1/3}Ti_{1/3})C$. *Ceram Int* 2026, **52**: 9217-9229.

[47] Ye B, Chu Y, Huang K, *et al.* Synthesis and characterization of $(Zr_{1/3}Nb_{1/3}Ti_{1/3})C$ metal carbide solid-solution ceramic. *J Am Ceram Soc* 2019, **102**: 919–923.

[48] Yang Q, Wang X, Bao W, *et al.* Influence of equiatomic Zr/(Ti,Nb) substitution on microstructure and ultra-high strength of (Ti,Zr,Nb)C medium-entropy ceramics at 1900 ℃. *J Adv Ceram* 2022, **11**: 1457–1465.

[49] Zhou X, Guo C, Yang Z, *et al.* Vacancy-induced mechanism on deformation and thermal conductivity in medium-entropy carbides with typical grain boundaries. *Mater Today Phy* 2026, **61**: 102025.

[50] Yu H, Liang W, Miao Q, *et al.* High temperature oxidation resistance and thermodynamic properties of (TaNbZr)N and (TaNbZr)C quaternary ceramic coating. *Corros Sci* 2024, **237**: 112315.

Just Accepted

[51] Miao Q, Fu Y, Chen H, *et al.* Simultaneous enhancement of mechanical and ablation properties of C/C composites modified by (Hf-Ta-Zr)C solid solution ceramics. *J Eur Ceram Soc* 2023, **43**: 3182–3190.

[52] Qin FL, Wang XG, Wang XF, *et al.* Sintering and High-Temperature Strength of (Ti,Hf,Ta)C Medium-Entropy Ceramics Consolidated by Biphasic Carbide Powders. *J Ceram Sci Technol* 2023, **14**: 39–48.

[53] Tang L, Pan Q, Yan K, *et al.* Competition between strong and weak carbide-forming elements in monolayer mixed oxide formation on (TiZrNbMoAl)C: Experimental and first-principles study. *Ceram Int* 2025, **51**: 26948–26959.

[54] Backman L, Opila EJ. Thermodynamic assessment of the group IV, V and VI oxides for the design of oxidation resistant multi-principal component materials. *J Eur Ceram Soc* 2019, **39**: 1796–1802.

[55] Yudin S, Sedegov A, Moskovskikh D, *et al.* Mechanism and kinetics of high-temperature oxidation of medium- and high-entropy carbides in air. *Mater Des* 2023, **231**: 112048.

[56] Wang H, Cao Y, Liu W, *et al.* Oxidation behavior of $(Hf_{0.2}Ta_{0.2}Zr_{0.2}Ti_{0.2}Nb_{0.2})$C-xSiC ceramics at high temperature. *Ceram Int* 2020, **46**: 11160–11168.

[57] Huang Z, Zhu Z, Su M, *et al.* High-temperature oxidation behaviors of dense TMC (TM= Ta, Nb, Ti and Zr) ceramics in air. *Ceram Int* 2023, **49**: 38036–38046.

[58] Mellor WM, Kaufmann K, Dippo OF, *et al.* Development of ultrahigh-entropy ceramics with tailored oxidation behavior. *J Eur Ceram Soc* 2021, **41**: 5791–5800.

[59] Backman L, Hunter BM, Weaver ML, *et al.* Invited Article: The oxidation kinetics and mechanisms observed during ultra-high temperature oxidation of (HfZrTiTaNb)C and (HfZrTiTaNb)$B_2$. *J Appl Phys* 2024, **136**: 05516.

[60] Shimada S, Onuma T, Kiyono H, *et al.* Oxidation of HIPed TiC ceramics in dry $O_2$, wet $O_2$, and $H_2O$ atmospheres. *J Am Ceram Soc* 2006, **89**: 1218–1225.

Just Accepted

[61] Zhang C, Loganathan A, Boesl B, *et al.* Thermal analysis of tantalum carbide-hafnium carbide solid solutions from room temperature to 1400 ℃. *Coatings* 2017, **7**: 111.

[62] Xu CH, Gao W. Pilling-Bedworth ratio for oxidation of alloys. Mat Res Innovat 2000, **3:** 231-235.

[63] Li Y, Gong J, Wu W, *et al.* Unveiling the high-temperature oxidation behavior of Ti-V-Nb-Mo-Al refractory high entropy alloy: A combined experimental and computational study. *Appl Surf Sci* 2026, **715**: 164555.

[64] Haggerty RP, Sarin P, Apostolov ZD, *et al.* Thermal expansion of $HfO_2$ and $ZrO_2$. *J Am Ceram Soc* 2014, **97**: 2213–2222.

[65] Patil RN, Subbarao EC. Axial thermal expansion of $ZrO_2$ and $HfO_2$ in the range room temperature to 1400℃. *J Appl Crystal* 1969, **2**: 281–288.

[66] Sugiyama K, Takeuchi Y. The crystal structure of rutile as a function of temperature up to 1600° C. *Crystal Mater* 1991, **194**: 305-313.

[67] Moldovan M, Weyant CM, Johnson DL, *et al.* Tantalum Oxide Coatings as Candidate Environmental Barriers. *J Therm Spray Techno* 2004, **13**: 51–56.

[68] Meng H, Chu Y. Surface energies in high-entropy carbides with variable carbon stoichiometry. *J Am Ceram Soc* 2022, **105**: 5835–5842.

[69] Fan Y, Chen Y, Wang J, *et al.* Insights into crystal growth and morphology evolution mechanism of multi-component carbide: Experiments and first-principles calculations. *J Mater Sci Technol* 2026, **240**: 27–34.

[70] Zhang Z, Yuan J, Li Z, *et al.* First-principles study on the surface oxidation behavior of ternary $M_6C_6$ ($M_6$ = $Zr_5Ti$, $Zr_5Ta$, $Hf_5Ti$, $Hf_5Ta$) carbides. *Comput Mater Sci* 2022, **210**: 111022.

[71] Li Y, He L, Pan H, *et al.* Compositional optimization for enhanced oxidation resistance of high-entropy carbide ceramics. *Acta Mater* 2025, **282**: 120463.

Just Accepted

[72] Luo H, Tang S, Liang C, *et al.* Correlation governs the impurity (Ti, Zr, Hf) diffusion in face−centered cubic iridium through first−principles calculation. *CALPHAD* 2022, **77**: 102433.

Just Accepted